

Article

Flying Target Detection Technology Based on GNSS Multipath Signals

Pengfei Zhu * , Qinglin Zhu, Xiang Dong and Mingchen Sun

China Research Institute of Radiowave Propagation, Qingdao 266107, China; zhuql1@crip.ac.cn (Q.Z.); dongx22s@163.com (X.D.); sunmc@crip.ac.cn (M.S.)

* Correspondence: zhupf@crip.ac.cn; Tel.: +86-0532-890-79203

Abstract: In this study, a passive radar system that detects flying targets is developed in order to solve the problems associated with traditional flying target detection systems (i.e., their large size, high power consumption, complex systems, and poor battlefield survivability). On the basis of target detection, the system uses the multipath signal (which is usually eliminated as an error term in navigation and positioning), enhances it by supporting information, and utilizes the multi-source characteristics of ordinary omnidirectional global navigation satellite system (GNSS) signals. The results of a validation experiment showed that the system is able to locate a passenger airplane and obtain its flight trajectory using only one GNSS receiving antenna. The system is characterized by its light weight (less than 5 kg), low power consumption, simple system, good portability, low cost, and 24/7 and all-weather work. It can be installed in large quantities and has good prospects for development.

Keywords: flying target; GNSS; multipath effect; passive radar

1. Introduction

Traditional flying target detection technology normally uses active radars to send ranging signals, and detects targets by analyzing the power, time delay, Doppler, and other characteristics of the echo signals [1,2]. However, this method requires the transmission of electromagnetic signals into the environment, which makes the system have a complex and bulky structure and high power consumption. In contrast, passive radars have simpler structures and lower power consumption because they do not actively transmit electromagnetic signals into the environment and only use external public signals as the signal source [3–7]. Additionally, passive radar systems do not require a complex structure for the signal-transmitting device, which allow them to be miniaturized and consume minimal power.

Global navigation satellite system (GNSS) signals have the advantages of global coverage, 24/7 and all-weather operation, and an open signal structure. Furthermore, in recent years, national navigation satellite systems have been developed rapidly, the number of global navigation satellites has become more abundant, and remote sensing technology using GNSS signals has become increasingly advanced. At present, this technology has realized engineering applications in the fields of sea surface altitude measurement [8,9], effective wave height measurement at sea level [10,11], the remote sensing of wind fields at sea level [12–15], the remote sensing of seawater salinity [16–18], and tidal detection [19–21]. In land surface remote sensing, numerous breakthroughs have also been made for measuring quantities such as soil moisture [22–24], snow thickness [25], and vegetation cover [26].

This paper develops a passive flight target detection system using GNSS signals as a signal source. The system utilizes the multipath signal, which is usually eliminated as an error term in navigation and positioning [27], as the basis for target detection, and is capable of realizing the localization of flying targets and the depiction of flight trajectories with the use of an ordinary omnidirectional GNSS antenna.



Citation: Zhu, P.; Zhu, Q.; Dong, X.; Sun, M. Flying Target Detection Technology Based on GNSS Multipath Signals. *Sensors* **2024**, *24*, 1706. <https://doi.org/10.3390/s24051706>

Academic Editor: Marco Diani

Received: 17 January 2024

Revised: 20 February 2024

Accepted: 26 February 2024

Published: 6 March 2024



Copyright: © 2024 by the authors. Licensee MDPI, Basel, Switzerland. This article is an open access article distributed under the terms and conditions of the Creative Commons Attribution (CC BY) license (<https://creativecommons.org/licenses/by/4.0/>).

A multipath signal is a signal that does not reach the receiving antenna through a direct path, but enters the receiving antenna after being reflected by a reflective surface [28–31]. According to the different levels of smoothness at different positions on the reflecting surface, the multipath signal can be divided into specular multipath and scattered multipath [29,32]. As shown in Figure 1, the specular multipath signal is formed by the reflection of a smooth reflective surface. This type of signal has a more regular carrier phase and higher intensity, and is the main source of interference in multipath interference. A scattered multipath signal is a dispersed signal reflection, meaning that the signal is a cluster of different phases and a superposition of different amplitudes. Consequently, a single direction of the wave signal is weaker, and is generally considered a common noise signal. Scattered multipath signals are often manifested as low-frequency noise attached to the direct signal, and the influence on the direct signal is much smaller than that on the specular reflection multipath signal.

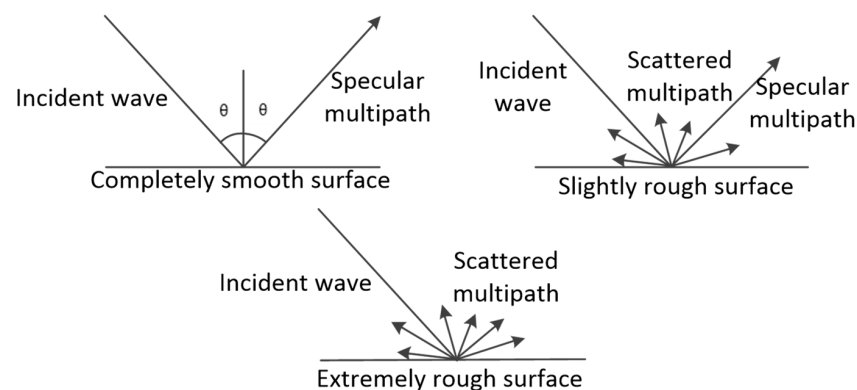


Figure 1. Specular and scattered multipath signals.

Conventional radar has two main methods of detecting flying targets: mechanical scanning and electrical scanning. Mechanical scanning involves the rotation of the radar antenna. Electrical scanning involves phased-array radar controls that change the direction of the radar beam by controlling the phase of the transmitted and received signals [33]. Both methods require complex system architectures and are expensive.

In contrast, the system developed in this study is a passive flying target detection system that uses GNSS signals as a signal source. The system utilizes the multipath signal (which is usually eliminated as an error term in navigation and positioning) as the basis for target detection, and utilizes the multi-source spread spectrum coding of GNSS signals and the superposition properties of specular multipath signals on direct signals to determine the position and trajectory of flying targets using an ordinary wide-beam omnidirectional GNSS antenna. The system is low-weight, easy to install, and undetectable, and consumes minimal power.

The rest of this paper is organized as follows. In Section 2.1, the model of multipath signals is presented. In Section 2.2, the detection range of GNSS signals is explained. Section 3.1 describes the experiment, and Section 3.2 discusses the results. Finally, Section 4 draws the conclusions of this study.

2. Materials and Methods

2.1. Signal Models

The reason why multipath signals have a greater impact on GNSS signals is that, unlike other noise interference signals, multipath signals have the same signal coding structure and almost the same carrier frequency as those of direct signals. Therefore, not only is the RF frontend unable to filter the multipath signal, but it also experiences difficulties in eliminating it in the signal digitization process.

The effect of the superposition of multipath signals on direct signals can be categorized into two types: enhancement superposition and offset superposition. In the case where

only a single multipath signal source is considered, the superposition effect shown in Figure 2 occurs.

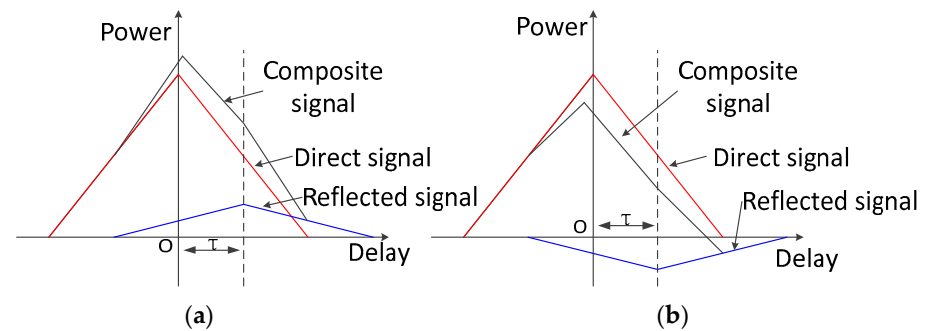


Figure 2. Effect of multipath signal superposition. (a) Superposition; (b) offset overlay.

As indicated in Figure 2, when the multipath signal has the same phase as or a similar phase to that of the direct signal, it has an enhanced superposition effect on the direct signal. When the multipath signal and the direct signal have opposite phases, the former has an offset superposition effect on the direct signal. For the superposition effect on the receiver, changes in the reflective surface and the relative position of the navigation satellite lead to the direct channel receiving signal strength fluctuations.

In the absence of multipath effect interference, the GNSS antenna directly receives the navigation signal from the GNSS satellite. After the steps involving RF frontend filtering, down-conversion, and power amplification are processed, the signal expression is

$$S_D(t) = \sqrt{2P_D}C(t)D(t)\cos[\omega t + \varphi_D(t)], \quad (1)$$

where S_D is the signal model in the case of no multipath interference, t is the signal reception time, P_D is the direct signal power, $C(t)$ denotes the coarse acquisition (C/A) code signal, $D(t)$ is the navigation message bit signal, ω is the carrier signal frequency, and $\varphi_D(t)$ is the initial carrier phase of the direct signal.

The GNSS signal propagation path after reflection from a flying target is shown in Figure 3. After being reflected by the target, part of the reflected signal is received by the GNSS receiver antenna according to the signal expression:

$$S_R(t) = \sqrt{2P_R}C(t - \tau)D(t - \tau)\cos[\omega t + \varphi_R(t)], \quad (2)$$

where P_R is the reflected signal power, τ is the time delay of the reflected signal with respect to the direct signal, and $\varphi_R(t)$ is the initial carrier phase of the reflected signal.

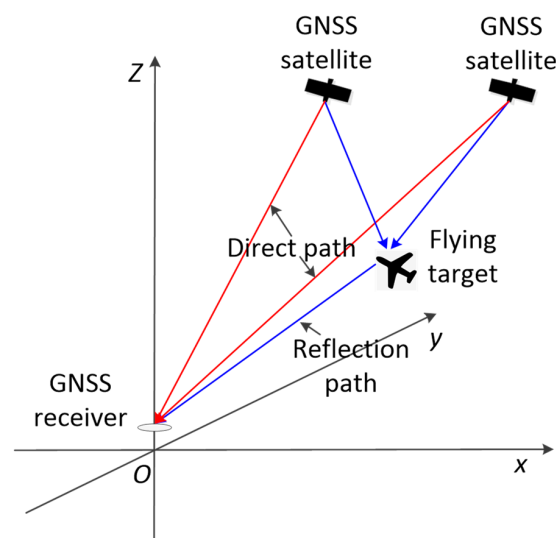


Figure 3. GNSS signal propagation path.

Without considering other multipath interference sources, the direct and reflected signals from the flying target are superimposed, and the signal is modeled as

$$S(t) = \sqrt{2P_D}C(t)D(t)\cos[\omega t + \varphi_D(t)] + \sqrt{2P_R}C(t - \tau)D(t - \tau)\cos[\omega t + \varphi_R(t)] + n(t) \quad (3)$$

where $n(t)$ is the noise signal power.

2.2. Detection Range

GNSS navigation and positioning systems use spread-spectrum coding techniques that provide a favorable suppression of multipath signals with delays greater than one code slice. However, when the delay is less than one code slice, the multipath signal will distort the correlation function between the received synthesized signal and the locally generated reference signal, which leads to a code tracking error in a delay-locked loop (DLL), and the signal-to-noise ratio of the tracking result increases. This property of the multipath effect of GNSS signals is utilized in this study to monitor the direct channel signals. Furthermore, when the multipath effect generated by the flying target generates a sudden and drastic change in the signal-to-noise ratio of a satellite signal, it indicates that the path delay of the specular multipath signals generated by the flying target is less than one code slice, and the flying target enters a region of known range. This range is an ellipsoidal region, with the positions of the GNSS-receiving antenna and the navigation satellite as the foci.

The coordinate system used in this study is shown in Figure 4, in which h is the flight altitude of the flying target and θ is the satellite elevation angle. $(-R/2, 0, 0)$ are the coordinates of the GNSS antenna, and $(R/2, 0, 0)$ are the coordinates of the navigation satellite.

$$\frac{x^2}{\left(\frac{R}{2}\right)^2} + \frac{y^2}{\left(\frac{R+r}{2}\right)^2 - \left(\frac{R}{2}\right)^2} + \frac{z^2}{\left(\frac{R+r}{2}\right)^2 - \left(\frac{R}{2}\right)^2} = 1. \quad (4)$$

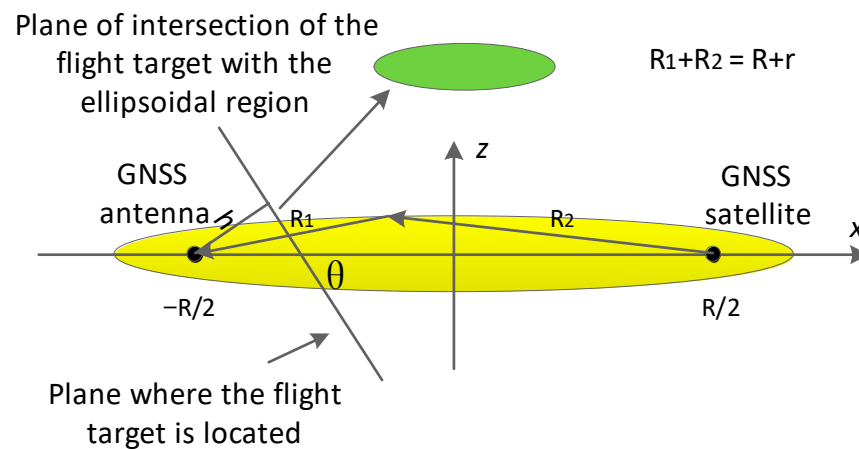


Figure 4. Coordinate system conversion.

The expression for the plane in which the flying target is located is

$$z = \frac{h}{\cos\theta} - \frac{R \tan\theta}{2} - \tan\theta x. \quad (5)$$

Inserting Equation (5) into Equation (4) enables the lengths of the long and short axes of the ellipsoid region formed by intersecting the ellipsoid at the height of the flying target to be calculated as follows:

$$A = \sqrt{(z_1 - z_2)^2 + (x_1 - x_2)^2} \quad (6)$$

$$B = R \sqrt{\frac{R^2(2Rr + r^2)}{16} - \left(\frac{h}{\sin\theta} - \frac{R}{2}\right)^2 \frac{2Rr + r^2}{4}} \quad (7)$$

where (x_1, z_1) and (x_2, z_2) are the coordinates of the two intersections between the long axis of the ellipse and the ellipsoid region.

In order to describe the range of the detection area more intuitively, the radar system was set up in accordance with the station center coordinate system. As shown in Figure 5, the coordinate system features the GNSS-receiving antenna as the origin, the zenith direction as the Z-axis, the due-east direction as the X-axis, and the due-north direction as the Y-axis, where R is the distance between the navigation satellite and the GNSS-receiving antenna, R_1 is the distance between the navigation satellite and the flying target, R_2 is the distance between the flying target and the GNSS-receiving antenna, and r is the transmission distance of a code slice time signal. When the position of the flying target satisfies the condition $R_1 + R_2 < R + r$, it enters the detection area (i.e., the yellow ellipsoidal region in the figure).

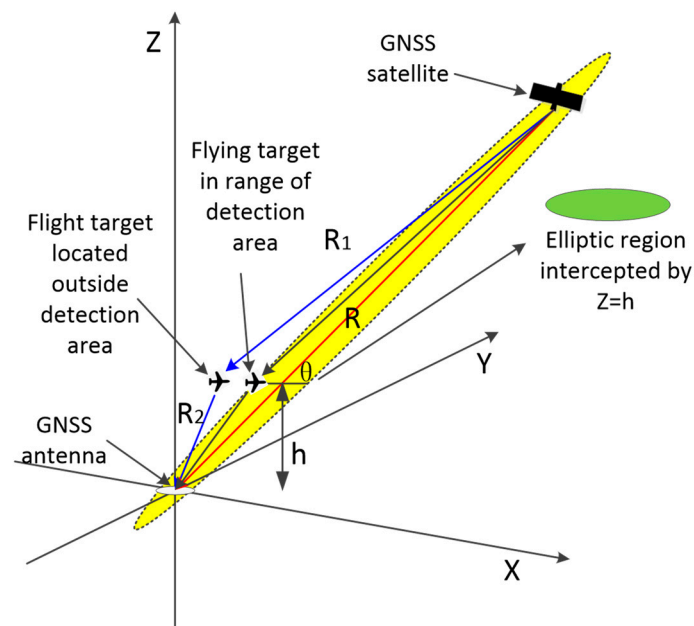


Figure 5. GNSS signal propagation model. The elliptical region represents the multipath detection area.

In the ellipsoid region, the GNSS antenna and navigation satellite are the two foci of the ellipsoid, h is the height of the flying target, and θ is the satellite elevation angle.

The upper and lower limits of the azimuth are, respectively,

$$\varphi_a = \varphi + \Delta\varphi = \varphi + \tan^{-1}\left(\frac{B}{2hcot\theta}\right) \quad (8)$$

$$\varphi_u = \varphi - \Delta\varphi = \varphi - \tan^{-1}\left(\frac{a}{2hcot\theta}\right) \quad (9)$$

where B is the short axis length, $\Delta\varphi$ is the maximum change in azimuth, and φ is the navigation satellite azimuth.

The upper and lower elevation limits are, respectively,

$$\vartheta_a = \theta + \tan^{-1}\left(\frac{z_1}{x_1 + \frac{R}{2}}\right) \quad (10)$$

$$\vartheta_u = \theta + \tan^{-1}\left(\frac{z_2}{x_2 + \frac{R}{2}}\right) \quad (11)$$

where (x_1, z_1) and (x_2, z_2) are the coordinates of the two intersections of the long axis of the ellipse with the ellipsoid region, and θ is the elevation angle of the navigation satellite.

The size of the ellipsoidal region formed by the intersection between the plane where the flying target is located and the ellipsoidal region is related to the satellite elevation angle and the height of the flying target. When the altitude of the flying target is fixed, the change in the detection area as a function of the elevation angle of the navigation satellite can be analyzed. We set the star-ground distance to $R = 25,000$ km and the flying target altitude to $h = 1$ km. The variations in the detection area of ellipsoids are shown in Figures 6–8.

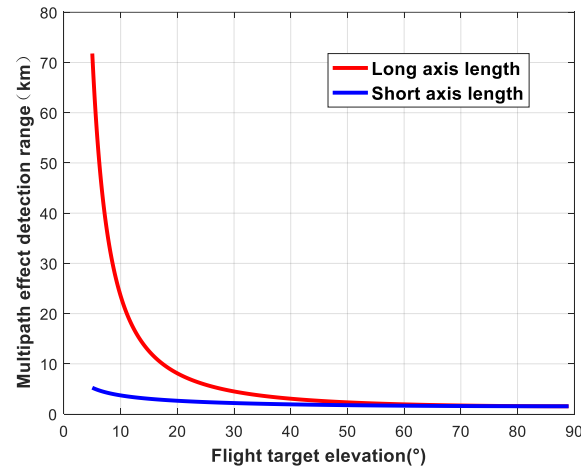


Figure 6. Variation in detection area as a function of satellite elevation (major and minor axes).

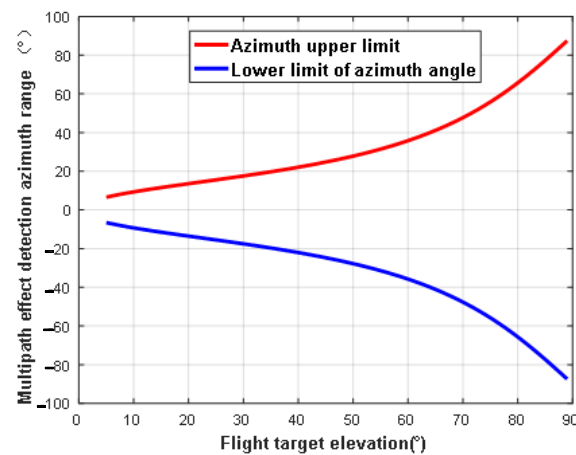


Figure 7. Variation in detection area change as a function of satellite elevation (azimuth).

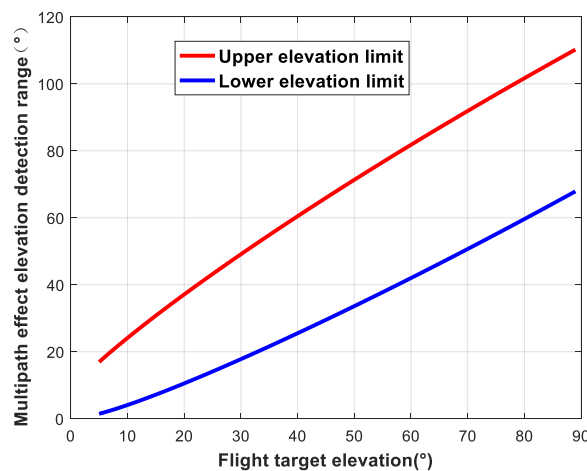


Figure 8. Variation in detection area as a function of satellite elevation (elevation).

When the elevation angle of the navigation satellite is fixed, the change in the detection area as a function of the altitude of the flying target can be analyzed. We set the star-ground distance to $R = 25,000$ km and the elevation angle of the navigation satellite to 30° . The variations in the detection area of ellipsoids are shown in Figures 9–11.

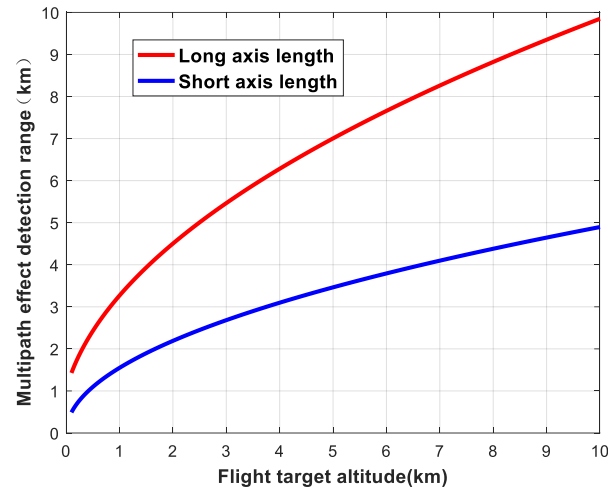


Figure 9. Variation in detection area as a function of flying target altitude (long and short axes).

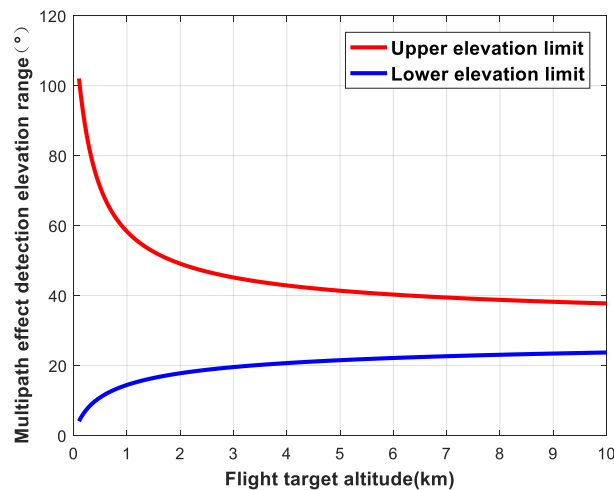


Figure 10. Variation in detection area as a function of flying target altitude (elevation).

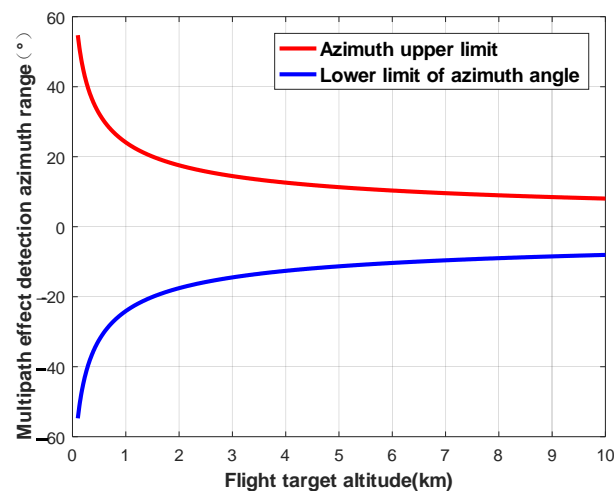


Figure 11. Variation in detection area as a function of flying target altitude (azimuth).

3. Results

3.1. Experiment

In order to verify the feasibility of the method, a passenger aircraft departing from Qingdao Liuting Airport was detected using signal receiving equipment. Qingdao Liuting Airport is located in Chengyang District of Qingdao City, is a class 4E civil international airport, and is one of the twelve major trunk airports in China. There is one main runway at the airport, and passenger airplanes usually take off in the southeast direction. The airport runway, flight path, and site of the experiment are shown in Figure 12.



Figure 12. Aerial view of the airport runway, flight path, and site of the experiment.

First, the test equipment was built at the southeast end of the runway. The experimental site was open. The experimental equipment was arranged as follows:

1. The antenna was set up in an open position facing the zenith direction;
2. The IF signal collector and signal-processing host were placed within a certain range of the antenna support;
3. The IF signal collector was connected to the PC computer cable, and the GNSS signal-receiving antenna was connected to the IF signal collector through the RF cable;
4. The video-recording equipment was set up to record the sky in the zenith direction.

The devices used in the experiment are shown in Table 1.

Table 1. Devices used in the experiment.

Num.	Device	Quantity
1	GNSS receiver antenna	1
2	Antenna bracket	1
3	RF cable	1
4	Video capture equipment	1
5	IF signal collector	1
6	Data storage hard drive	1
7	Data processing terminal	1

The site of the experiment and the experimental setup are shown in Figure 13.

After the test equipment was built, the host computer was turned on, the signal acquisition software was initialized, and the IF data storage location was selected.

After the flying target flew over the receiving antenna, the appearance, passing vertex, and departure time of the flying target were recorded. Afterwards, the recorded results were compared with the video to ensure their accuracy. The information recorded during the experiment is displayed in Table 2.

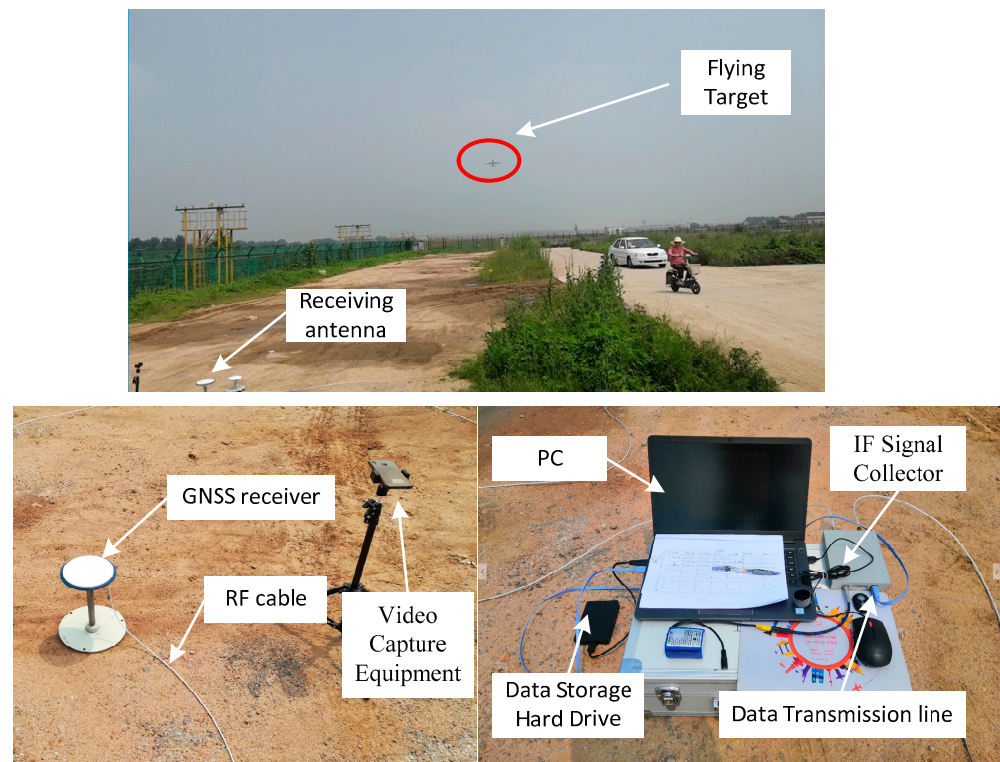


Figure 13. Site of the experiment and experimental setup.

Table 2. Data recorded during the experiment.

Num.	Event	Absolute Time	Relative Time (s)
1	Start Collection	10:14:00	0
2	Target Appearance	10:14:41	41
3	Target Over Top	10:14:51	51
4	Target Leaving	10:15:12	72
5	Stop Collection	10:16:30	150
6	Start Collection	10:16:30	0
7	Target Appearance	10:17:59	89
8	Target Over Top	10:18:08	98
9	Target Leaving	10:18:27	117
10	Stop Collection	10:19:00	150

3.2. Analysis of Results

After the experiment was completed, the intermediate frequency data were captured and tracked, the coordinates of the experimental site and navigation satellite were calculated, and a starry sky map of the site was drawn, as shown in Figure 14.

In Figure 14, the spokes represent different azimuth angles, the concentric circles represent different elevations, and the solid dots represent the locations of the GNSS satellites. The detection ranges of different satellite signals are based on the satellite elevation and azimuth angles, as shown in Figure 15.

In Figure 15, the elliptical areas with different colors correspond to the detection ranges of the navigation satellites. In the experiment, when the flying target passed over the GNSS antenna's zenith, the estimated positions of the satellites present at the time were determined, as shown in Figure 16.

The changes in the signal-to-noise ratios of different satellites were used to determine the satellite timing sequence of the flying target as it crossed the detection range of different satellites, and the trajectory of the flying target could be obtained as a result. As shown in Figure 17.

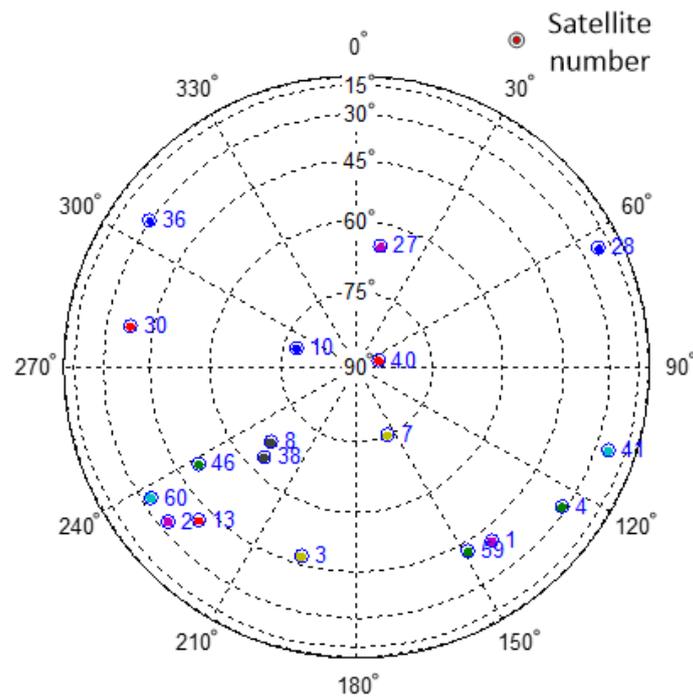


Figure 14. Starry sky map. Different colored dots represent different satellites.

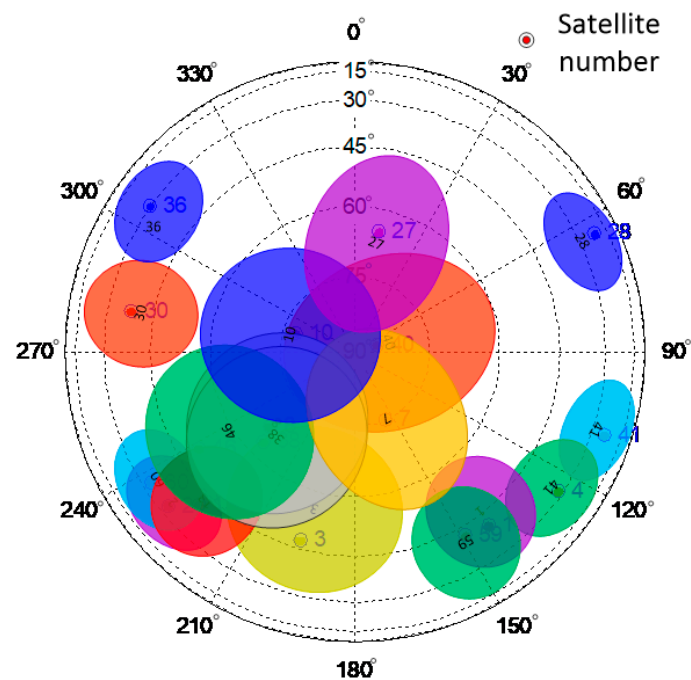


Figure 15. Schematic diagram of detection area for each GNSS satellite. Different colored dots and ovals represent different satellites and the multipath detection range of the satellite.

In the first experiment, according to the carrier-to-noise ratio data, when the relative times were 44.9 s, 45.65 s, and 46.4 s, the flying target passed through the multipath detection areas of satellites 27, 40, and 7, respectively. In the second experiment, according to the carrier-to-noise ratio data, when the relative times were 92.29 s, 93.21 s, and 93.99 s, the flying target passed through the multipath detection areas of satellites 27, 40, and 7, respectively. Using this information, the trajectory of the flying target was drawn, as shown in Figure 18. The trajectory of the flying target was consistent with the actual flight path of the flying target shown in Figure 12.

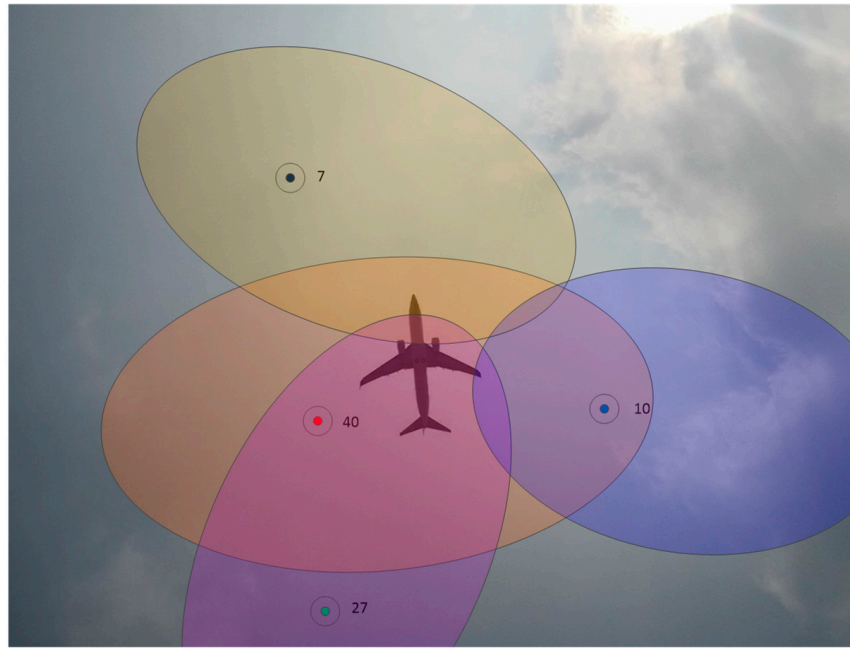


Figure 16. Starry sky map of the experiment as the flying target passed over the GNSS antenna’s zenith. Different colored dots and ovals represent different satellites and the multipath detection range of the satellite.

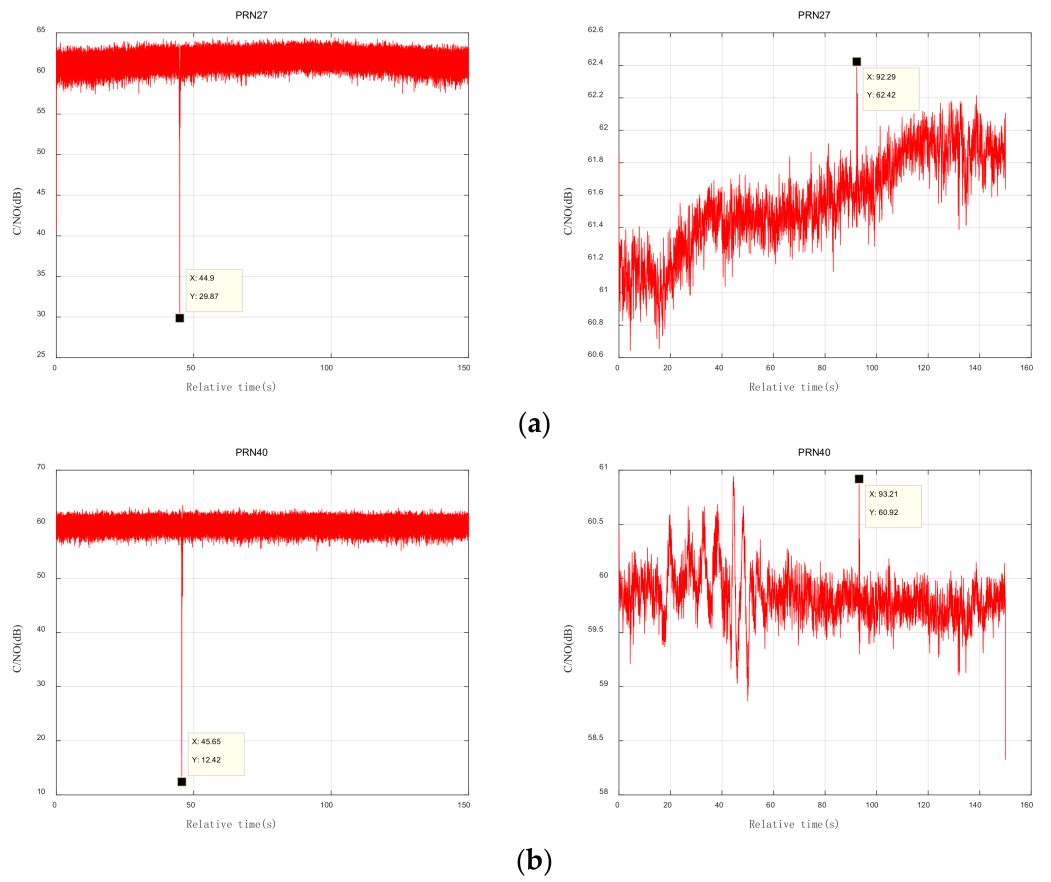


Figure 17. Cont.

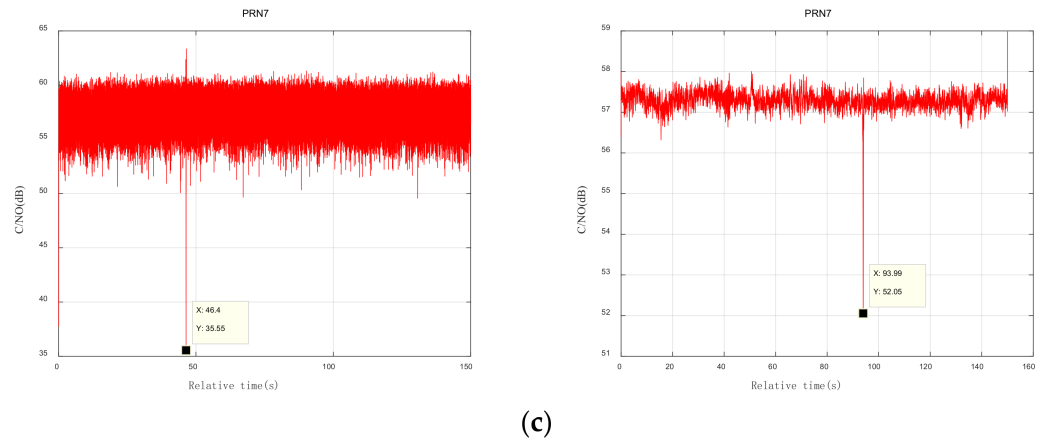


Figure 17. Carrier-to-noise ratio calculations. (a) Variation in signal-to-noise ratio of satellite 27 signals; (b) variation in signal-to-noise ratio of satellite 40 signals; (c) variation in signal-to-noise ratio of satellite 7 signals.

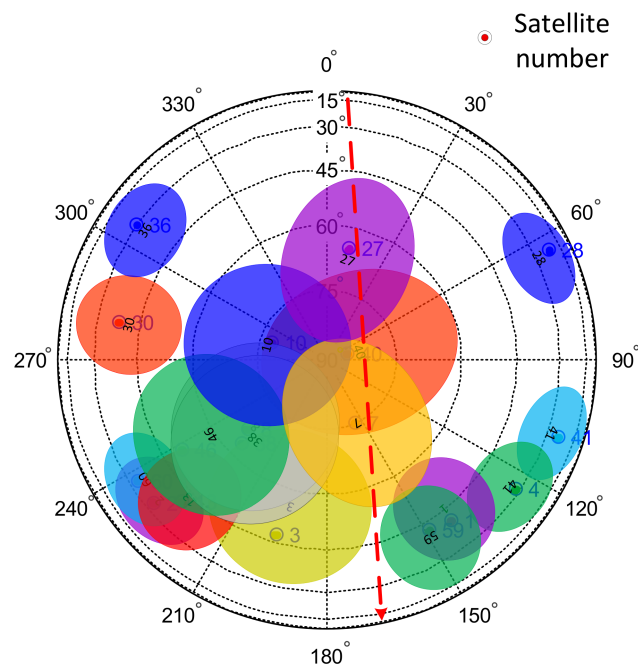


Figure 18. Estimation of the trajectory of the flying target. The red dashed arrow represents the direction of flight of the flying target, and different colored dots and ovals represent different satellites and the multipath detection range of the satellite.

4. Conclusions

In this study, we described in detail the technical principles of GNSS-based multipath signals for the detection of flying targets, and we conducted an experiment at Qingdao Liuting Airport to verify the feasibility of the technical solution. The results demonstrate that the use of passive radar technology enables the determination of trajectories of targets that are difficult to detect; it also enables low-cost systems with structural simplicity, portability, and minimal power consumption to be utilized. In recent years, the increasing number of small aircrafts, such as drones, gliders, and small helicopters, has added to the difficulties of the safety management of urban airspace and other important airspaces. Traditional small aircraft detection methods mainly include radar detection, photoelectric detection, acoustic wave detection, etc. However, radar systems are complex, large, power-hungry and costly, optoelectronic devices are greatly affected by weather, and acoustic devices are susceptible to interference and have poor accuracy. In follow-up work, we hope

to be able to apply this technology to the detection and management of small aircrafts. Additionally, because the hardware environment is not currently available for the real-time detection of flying targets, the main aim of future work will be to build a hardware system that detects flying targets in real time.

Author Contributions: Conceptualization, P.Z.; methodology, P.Z.; software, P.Z. and X.D.; validation, P.Z.; formal analysis, P.Z.; investigation, P.Z.; resources, Q.Z. and X.D.; data curation, P.Z.; writing—original draft preparation, P.Z.; writing—review and editing, P.Z. and M.S.; visualization, P.Z.; supervision, Q.Z.; project administration, X.D.; funding acquisition, Q.Z. All authors have read and agreed to the published version of the manuscript.

Funding: This research received no external funding.

Institutional Review Board Statement: Not applicable.

Informed Consent Statement: Not applicable.

Data Availability Statement: The data set is available on request to the corresponding authors.

Acknowledgments: We thank the staff of Liuting Airport for their cooperation.

Conflicts of Interest: The authors declare no conflicts of interest.

References

1. Bao, Z.; Xing, M.; Wang, T. *Radar Imaging Technology*; Electronic Industry Press: Beijing, China, 2005.
2. Huang, P.; Yin, H.; Xu, X. *Radar Target Characteristics*; Electronic Industry Press: Beijing, China, 2005.
3. White, S. Passive Radar. *Pract. Wirel.* **2021**, *97*, 14–15.
4. Yu, Q.; Peng, H.; Sun, Z.; Wu, Y. Target Detection Technology Based on Signals of Multiple Transponders on Broadcasting Satellite. *Telecommun. Eng.* **2016**, *56*, 140–144.
5. Park, G.H.; Kim, H.N. Convolutional Neural Network-based Target Detection Method for Passive Bistatic Radar using FM Broadcasting Signals. *J. Inst. Electron. Inf. Eng.* **2020**, *57*, 70–78.
6. Tang, H.; Wan, X.R.; Chen, W.; Ke, H. Experimentation on Target Detection with Passive Radar Based on Digital Terrestrial Multimedia Broadcasting. *J. Electron. Inf. Technol.* **2014**, *35*, 575–580. [[CrossRef](#)]
7. Wang, X.-R. An Overview on Development of Passive Radar Based on the Low Frequency Band Digital Broadcasting and TV Signals. *J. Radars* **2012**, *1*, 109–123.
8. Martin-Neira, M.; Caparrini, M.; Font-Rossello, J.; Lannelongue, S.; Vallmitjana, C.S. The PARIS concept: An experimental demonstration of sea surface altimetry using GPS reflected signals. *IEEE Trans. Geosci. Remote Sens.* **2001**, *39*, 142–150. [[CrossRef](#)]
9. Zhang, Y.; Huang, S.; Han, Y.; Yang, S.; Hong, Z.; Ma, D.; Meng, W. Machine learning methods for spaceborne GNSS-R sea surface height measurement from TDS-1. *IEEE J. Sel. Top. Appl. Earth Obs. Remote Sens.* **2021**, *15*, 1079–1088. [[CrossRef](#)]
10. Wang, D.; Sun, Y.; Wang, X.; Bai, W.; Du, Q.; Xia, J.; Han, Y. A New GNSS-R Interferometric Ocean Altimetry Using Beidou-3 Signal. *Chin. J. Space Sci.* **2022**, *42*, 492–499. [[CrossRef](#)]
11. Bu, J.; Yu, K.; Park, H.; Huang, W.; Han, S.; Yan, Q.; Qian, N.; Lin, Y. Estimation of Swell Height Using Spaceborne GNSS-R Data from Eight CYGNSS Satellites. *Remote Sens.* **2022**, *14*, 4634. [[CrossRef](#)]
12. Bu, J.; Yu, K.; Zuo, X.; Ni, J.; Li, Y.; Huang, W. GloWS-Net: A Deep Learning Framework for Retrieving Global Sea Surface Wind Speed Using Spaceborne GNSS-R Data. *Remote Sens.* **2023**, *15*, 590. [[CrossRef](#)]
13. Hoseini, M.; Nahavandchi, H. The potential of spaceborne GNSS reflectometry for detecting ocean surface currents. *Remote Sens. Environ.* **2022**, *282*, 113256. [[CrossRef](#)]
14. Li, C.; Huang, W. An algorithm for sea-surface wind field retrieval from GNSS-R delay-Doppler map. *IEEE Geosci. Remote Sens. Lett.* **2014**, *11*, 2110–2114.
15. Jing, C.; Niu, X.; Duan, C.; Lu, F.; Di, G.; Yang, X. Sea Surface Wind Speed Retrieval from the First Chinese GNSS-R Mission: Technique and Preliminary Results. *Remote Sens.* **2019**, *11*, 3013. [[CrossRef](#)]
16. Kainulainen, J.; Rautiainen, K.; Hallikainen, M.; Takala, M. Radiometric performance of interferometric synthetic aperture radiometer HUT-2D. In Proceedings of the IEEE International Geoscience & Remote Sensing Symposium, Boston, MA, USA, 6–11 July 2008.
17. Kainulainen, J.; Rautiainen, K.; Lemmetyinen, J.; Hallikainen, M.T.; Martin-Porqueras, F.; Martin-Neira, M. Detection of a sea surface salinity gradient using data sets of airborne synthetic aperture radiometer HUT-2-D and a GNSS-R instrument. *IEEE Trans. Geosci. Remote Sens.* **2011**, *49*, 4561–4571. [[CrossRef](#)]
18. Valencia, E.; Camps, A.; Rodriguez-Alvarez, N.; Ramos-Perez, I.; Bosch-Lluis, X.; Park, H. Improving the accuracy of sea surface salinity retrieval using GNSS-R data to correct the sea state effect. *Radio Sci.* **2011**, *46*, 1–11. [[CrossRef](#)]
19. Tabibi, S.; Geremia-Nievinski, F.; Francis, O.; van Dam, T. Tidal analysis of GNSS reflectometry applied for coastal sea level sensing in Antarctica and Greenland. *Remote Sens. Environ.* **2020**, *248*, 111959. [[CrossRef](#)]

20. Semmling, A.M.; Beyerle, G.; Stosius, R.; Dick, G.; Wickert, J.; Fabra, F.; Cardellach, E.; Ribó, S.; Rius, A.; Helm, A.; et al. Detection of Arctic Ocean tides using interferometric GNSS-R signals. *Geophys. Res. Lett.* **2011**, *38*, 6005. [[CrossRef](#)]
21. Ban, W.; Zhang, K.; Yu, K.; Zheng, N.; Chen, S. Detection of red tide over sea surface using GNSS-R spaceborne observations. *IEEE Trans. Geosci. Remote Sens.* **2022**, *60*, 5802911. [[CrossRef](#)]
22. Wu, X.; Ma, W.; Xia, J.; Bai, W.; Jin, S.; Calabria, A. Spaceborne GNSS-R Soil Moisture Retrieval: Status, Development Opportunities, and Challenges. *Remote Sens.* **2021**, *13*, 45. [[CrossRef](#)]
23. Jia, Y.; Jin, S.; Savi, P.; Yan, Q.; Li, W. Modeling and Theoretical Analysis of GNSS-R Soil Moisture Retrieval Based on the Random Forest and Support Vector Machine Learning Approach. *Remote Sens.* **2020**, *12*, 3679. [[CrossRef](#)]
24. Rodríguez-Alvarez, N.; Bosch-Lluis, X.; Camps, A.; Vall-llossera, M.; Valencia, E.; Marchan-Hernandez, J.F.; Ramos-Perez, I. Soil moisture retrieval using GNSS-R techniques: Experimental results over a bare soil field. *IEEE Trans. Geosci. Remote Sens.* **2009**, *47*, 3616–3624. [[CrossRef](#)]
25. Zhang, Y.; Gu, W.; Han, Q.; Cao, Y.; Xia, Y.; Wang, Q. Research of dry snow depth detection based on GNSS-R. *Electron. Des. Eng.* **2015**, *11*, 64–73.
26. Rodríguez-Alvarez, N.; Monerris, S.; Bosch-Lluis, X.; Camps, A.; Marchan-Hernandez, J.F.; Ramos-Perez, I.; Valencia, E.; Vall-Llossera, M.; Nieto, J.M. *Soil Moisture Retrieval Using GNSS-r: Vegetation Effects*; SMOS Barcelona Expert Centre: Passeig Marítim de la Barceloneta, Spain, 2017; pp. 37–49.
27. Zhang, M.; Zhang, J. A Fast Satellite Selection Algorithm: Beyond Four Satellites. *IEEE J. Sel. Top. Signal Process.* **2009**, *3*, 740–747. [[CrossRef](#)]
28. Keshvadi, H.; Broumandan, A.; Lachapelle, G. Spatial Characterization of GNSS Multipath Channels. *Int. J. Antennas Propag.* **2012**, *2012*, 236464. [[CrossRef](#)]
29. Feng, X.; Jin, G.; Fan, J.; Wu, X. Experimentation and analysis of multipath effect in pseudo-range measurement of GNSS receiver. *Mod. Electron. Tech.* **2013**, *5*, 77–81.
30. Wang, S. Detection and Analysis of GNSS Multipath. Master's Thesis, KTH Royal Institute of Technology School of Architecture and the Built Environment, Tockholm, Sweden, 2016.
31. Han, S.; Wu, B.; Wang, G.; Yin, Z. Research on Position-Domain GNSS Multipath Error Modelling Method Based on Sidereal Filtering. In Proceedings of the China Satellite Navigation Conference, Chengdu, China, 22–25 November 2020.
32. Xiao, Y.; Zheng, G.; Gong, J.; Guo, Y. Analysis of Low-altitude Target Tracking Indication Angle Error Caused by Specular Multipath. *J. Proj. Rocket. Missiles Guid.* **2016**, *36*, 9–12.
33. Budge, M.C.; German, S.R. *Basic Radar Analysis*; Artech House: London, UK, 2020.

Disclaimer/Publisher's Note: The statements, opinions and data contained in all publications are solely those of the individual author(s) and contributor(s) and not of MDPI and/or the editor(s). MDPI and/or the editor(s) disclaim responsibility for any injury to people or property resulting from any ideas, methods, instructions or products referred to in the content.